Research Square

Preprints are preliminary reports that have not undergone peer review.
They should not be considered conclusive, used to inform clinical practice,
or referenced by the media as validated information.

Spin-orbit torque driven antiferromagnetic oscillator

Joerg Wunderlich

joerg.wunderlich@physik.uni-regensburg.de

Institute of Experimental and Applied Physics, University of Regensburg https://orcid.org/0000-0003-2631-828X

Pradeep Rout

Institute of Experimental and Applied Physics, University of Regensburg

Joao Godinho

Institute of Experimental and Applied Physics, University of Regensburg

Franz Vilsmeier

Fakultaet fur Physik, Technische Universitaet Muenchen, 85748 Garching, Germany https://orcid.org/0000-0002-5648-3051

Ruslan Salikhov

Helmholtz Zentrum Dresden Rossendorf https://orcid.org/0000-0001-8461-0743

Javier Velez

Donostia International Physics Center, 20018 San Sebastian, Spain

Zbynek Soban

Institute of Physics ASCR https://orcid.org/0000-0002-8751-931X

David Laroze

Donostia International Physics Center, 20018 San Sebastian, Spain

Olena Gomonay

Johan Guttenberg University https://orcid.org/0000-0002-9413-0337

Ruben M. Otxoa

Hitachi-Cambridge Laboratory https://orcid.org/0000-0003-1534-4159

Christian Back

Technical University Munich https://orcid.org/0000-0003-3840-0993

Olav Hellwig

Chemnitz University of Technology https://orcid.org/0000-0002-1351-5623

Article

Keywords:

Posted Date: April 5th, 2026

DOI: https://doi.org/10.21203/rs.3.rs-7649904/v1

License: This work is licensed under a Creative Commons Attribution 4.0 International License.
Read Full License

Additional Declarations: There is **NO** Competing Interest.

Spin-orbit torque driven antiferromagnetic oscillator

P. K. Rout,[1] J. Godinho,[1] F. Vilsmeier,[2] R. Salikhov,[3] J. A. Vélez,[4,5] Z. Šobáň,[6] D. Laroze,[7] O. Gomonay,[8] R. M. Otxoa,[9,4] C. H. Back,[2] O. Hellwig,[3,10] and J. Wunderlich[1,6]

[1]*Institute of Experimental and Applied Physics, University of Regensburg, Universitässtrasse 31, 93051 Regensburg, Germany*

[2]*Fakultät fur Physik, Technische Universität München, 85748 Garching, Germany*

[3]*Institute of Ion Beam Physics and Materials Research, Helmholtz-Zentrum Dresden-Rossendorf, Bautzner Landstrasse 400, 01328 Dresden, Germany*

[4]*Donostia International Physics Center, 20018 San Sebastián, Spain*

[5]*Polymers and Advanced Materials Department: Physics, Chemistry, and Technology, University of the Basque Country, UPV/EHU, 20018 San Sebastián, Spain*

[6]*Institute of Physics, Czech Academy of Sciences, Cukrovarnická 10, 162 00, Praha 6, Czech Republic*

[7]*Instituto de Alta Investigación, Universidad de Tarapacá , Casilla 7D, 1000000, Arica, Chile.*

[8]*Institute of Physics, Johannes Gutenberg-University Mainz, 55128 Mainz, Germany.*

[9]*Hitachi Cambridge Laboratory, Cambridge CB3 0HE, United Kingdom*

[10]*Institute of Physics, Chemnitz University of Technology, Reichenhainer Strasse 70, 09107 Chemnitz, Germany*

Antiferromagnets offer a promising pathway toward robust and ultrafast spintronic devices due to their intrinsically zero net magnetic moment and exchange-enhanced spin dynamics. Here, we demonstrate a spin-orbit torque (SOT)-driven oscillator based on a nanoconstriction patterned from a synthetic antiferromagnet (SAF). Spin rectification measurements reveal SOT-driven excitations of both optical and acoustic modes, along with additional resonances that emerge above a threshold DC current near the spin-flop transition. These resonances originate from self-sustained oscillations whose chirality is determined by the polarity of the driving DC current, and which can injection-lock to the detection frequency. Macrospin and micromagnetic simulations corroborate the existence of these chiral self-oscillations and predict chaotic dynamics near the spin-flop regime, experimentally indicated as the sudden onset of multiple oscillation modes above a DC threshold current.

Spin-transfer torque (STT) and spin–orbit torque (SOT) nano-oscillators are at the forefront of spintronics research due to their potential applications in neuromorphic computing, microwave-assisted magnetic recording, magnonics, and wireless communications [1–6]. They have attracted considerable attention for their flexible device geometry, CMOS compatibility and robust mutual synchronization [4, 5, 7, 8]. STT nano-oscillators typically employ nanoscale spin valves or magnetic tunnel junctions, in which spin-polarized currents compensate magnetic damping to sustain microwave oscillations. Their frequencies are primarily determined by the applied magnetic field magnitude, and their inherently right-handed chirality is locked to the magnetic field orientation [9–15]. Similarly, SOT nano-oscillators drive magnetization precession through charge-to-spin current conversion [16–21]. When based on ferromagnets, both STT and SOT oscillators exhibit limited controllability: at a fixed applied magnetic field, their right-handed chirality remains fixed, and their frequency can only be tuned slightly e.g., via voltage-controlled magnetic anisotropy [22, 23].

Very promising alternative concepts for spintronic oscillators based on antiferromagnets have been theoretically proposed, combining ultrafast, exchange-enhanced spin dynamics that push oscillator frequencies into the THz regime with bias-current control over both frequency and chirality [24–30]. This includes chiral self-oscillations as well as resonantly

driven left- and right-handed circularly polarized modes in easy-axis systems, and linearly polarized resonant acoustic and optical modes in easy-plane antiferromagnets [28, 29, 31, 32]. Moreover, the dynamical range for sustaining self-oscillations is predicted to be significantly broader than in ferromagnetic oscillators [33]. For example, chiral self-sustained Néel-order oscillations spanning the entire frequency range between the acoustic and optical eigenmodes have been predicted when an insulating antiferromagnet is excited by spin currents generated in an adjacent nonmagnetic metal layer [24]. One particularly compelling concept envisions spin–orbit torque-driven self-oscillations directly in a metallic parity-time (PT)-symmetric antiferromagnet [25]. In these conductive systems, self-oscillations and their chirality can be detected via phase-sensitive nonlinear rectification, arising from time-dependent magneto-transport phenomena such as anisotropic magnetoresistance (AMR) or the anomalous Hall effect (AHE) as found in noncollinear antiferromagnets [34, 35].

In addition to periodic excitations, antiferromagnetic oscillators are predicted to exhibit chaotic behavior when driven near the critical spin-flop transition [26, 27]. Such chaotic behavior, unprecedented in ferromagnetic oscillators yet reminiscent of vortex-based oscillator dynamics driven by feedback and core reversal, could open new opportunities for neuromorphic reservoir computing [36, 37].

In this work, we investigate both resonant eigenmodes and self-sustained oscillations in a synthetic antiferromagnet (SAF) multilayer, which serves as a highly simplified yet versatile antiferromagnetic system. Despite its structural simplicity, the SAF retains all the essential ingredients required to support complex current-driven antiferromagnetic dynamics. Our SAF consists of two ferromagnetic layers separated by a nonmagnetic spacer that mediates a Ruderman–Kittel–Kasuya–Yosida (RKKY) interaction, resulting in antiferromagnetic coupling between the layers [38]. Furthermore, the SAF is sandwiched between a tantalum (Ta) seed and platinum (Pt) cap layer, which possess opposite spin Hall angles. When a charge current flows through the multilayer stack, the heavy-metal interfaces generate spin currents that are injected into the SAF from both sides with identical spin polarization [39–41]. The resulting spin–orbit torque (SOT) acts on the antiferromagnetic order of the SAF in a manner analogous to the theoretically studied spin-transfer torque (STT) in collinear antiferromagnets, where chaotic self-oscillatory dynamics are predicted near the spin-flop transition [26].

By driving the SAF with current induced SOT, we observe both the expected antiferromagnetic eigenmodes as well as self-oscillations. Using a combination of radio-frequency (RF) current excitation and an in-plane magnetic field with tunable magnitude and orientation, we detect linearly polarized acoustic and optical resonance modes through the spin rectification effect (SRE) [34, 42, 43]. Additional rectification peaks appear in the magnetic field dependence of the SRE signal when the applied DC current exceeds a critical threshold. These resonances are attributed to self-sustained chiral excitations of the antiferromagnetic order, which become injection-locked to the frequency of the RF signal. While the SRE signal amplitude increases monotonically with DC current magnitude above the threshold, the current polarity-dependent sign of the SRE signal confirms that the oscillation chirality is locked to the direction of the driving DC current.

To verify the presence of SOT-driven self-oscillations, we conducted macrospin and micromagnetic simulations based on experimental material parameters and device geometry. Near the critical spin-flop transition of the SAF, the simulations reproduce current-induced self-oscillations spanning a broad frequency range. Consistent with experimental observations, the simulations confirm also injection locking of these self-oscillations to the frequency of the applied RF probing current. Furthermore, Lyapunov exponent analyses and bifurcation diagrams from the macrospin simulations reveal the emergence of chaotic dynamics in the DC-driven self-oscillations of the SAF.

1. Spin-orbit torque-driven excitation of SAF eigenmodes

To probe the spin dynamics of the SAF nanoconstriction, we applied a radio-frequency (RF) current and measured the resulting spin rectification voltage V_{SRE} while sweeping an in-plane magnetic field. This voltage originates from nonlinear mixing of the time-dependent resistance, modulated by anisotropic magnetoresistance (AMR) and giant magnetoresistance (GMR), and the RF current. The rectification generates a second-order DC signal V_{SRE}, along with a high-frequency component at 2ω [34, 42, 43].

The SAF multilayer stack (Fig. 1a) comprises two 2-nm-thick permalloy (Py : $Ni_{0.81}Fe_{0.19}$) layers, antiferromagnetically coupled through a 0.34-nm Ir spacer via the RKKY interaction. To enhance current density and spatially confine the magnetic excitations, the stack

was patterned into a bar featuring a single notch-shaped nanoconstriction (Fig. 1b). Vibrating sample magnetometry (VSM) reveals a predominant easy-plane magnetic anisotropy (Supplementary Section 1). An additional weak in-plane biaxial anisotropy is induced by the nanofabrication (Supplementary Section 2).

Applying an in-plane magnetic field induces a net magnetization ($\vec{M}_1 + \vec{M}_2$) aligned with the field, and a Néel vector ($\vec{M}_1 - \vec{M}_2$) oriented perpendicular to it. Which mode is excited depends on the azimuthal angle Φ between the applied field and the RF current set by the bar orientation. In the acoustic mode, the field-induced magnetization precesses with constant magnitude around the direction of the applied field, whereas in the optical mode, the induced magnetization periodically varies its magnitude while maintaining its orientation along the field. As illustrated in Fig. 1c, the acoustic and optical modes can be selectively or jointly excited depending on Φ, consistent with the symmetry of the spin-orbit torque excitation. Fig. 1d shows distinct resonance peaks corresponding to the acoustic and optical eigenmodes of the SAF at 8 GHz, which arise from in-plane and out-of-plane oscillation of the net-magnetization, respectively. These excitations are driven by spin–orbit torques generated at the Pt (top) and Ta (bottom) interfaces via the spin Hall effect. Due to their opposite spin Hall angles, both heavy-metal layers inject spin currents of identical polarization into the SAF from opposite sides. When the field is applied parallel to the current ($\Phi = 0^o$), only the acoustic mode is excited, as seen by the resonance peak at positive field polarity. The absence of a corresponding resonance at negative field is attributed to a pinned 180° domain wall at the nanoconstriction, which cancels the SRE contributions from oppositely magnetized domains (Supplementary Section 3; this domain-wall pinning phenomenon will be discussed in detail in a forthcoming publication on chiral eigenmode excitation of individual antiferromagnetic domains). A slight misalignment (e.g., $\Phi = 5^o$) restores acoustic resonances at both field polarities, indicating a uniform magnetic state. At $\Phi = 45^o$, both acoustic and optical modes are observed. For $\Phi = 90^o$, only the optical mode is excited. At opposite oriented applied magnetic fields the sign of the SRE signal is inverted indicating that the rectification arises primarily from damping-like SOT, with negligible contributions from field-like torque or Oersted fields [43]. The opposite signs of the acoustic and optical peaks at the same field polarity further suggest different dominant rectification mechanisms: AMR for the acoustic mode and GMR for the optical mode.

At higher field magnitudes, Joule heating can introduce additional components to the detected signal through magneto-thermoelectric effects. In particular, a background voltage offset arises from the anomalous Nernst effect (ANE), which is driven by a vertical temperature gradient combined with a net magnetization component perpendicular to the bar. This net magnetization appears when the applied magnetic field tilts the two antiferromagnetically coupled layers such that a perpendicular component develops (see Fig. 1d for $\Phi = 90^o$ and $\Phi = 45^o$, and Supplementary Section 4).

Fig. 1e shows the frequency dependence of the acoustic mode: the resonance shifts to higher magnetic fields as the RF frequency increases, in agreement with the theoretical expectation. In Fig. 1f, we compare the experimental resonance fields with the analytical expressions for easy-plane antiferromagnets. The acoustic mode follows $f_{acoustic} = \gamma H(1 + |H_{an}|/2H_{ex})^{1/2}$, and the optical mode $f_{optical} = \gamma\{2H_{ex}|H_{an}|$ - $(|H_{an}|/2H_{ex})H^2\}^{1/2}$ where H_{ex} and H_{an} corresponds to the antiferromagnetic RKKY exchange field and anisotropy field respectively. Using independently determined values $\mu_0 H_{ex} = 0.25$ T and $\mu_0 H_{an} = 0.98$ T from VSM measurements (Supplementary Section 1), we find excellent agreement between experiment and theory.

2. Micromagnetic simulation of chiral self-oscillations

To gain further insight into the current-driven spin dynamics observed in the SAF nanoconstriction, we performed micromagnetic simulations using the GPU-accelerated open-source solver MuMax3 (see Methods) [44]. While micromagnetic simulations neglect exchange damping, an effect that becomes relevant in true antiferromagnets with strong atomic-scale exchange interactions, they remain well-suited for studying SAF systems composed of ferromagnetic layers. In such multilayers, the local magnetizations are antiferromagnetically coupled only through the comparatively weak RKKY interaction across a non-magnetic spacer, which justifies treating their dynamics within a conventional micromagnetic framework [45–47].

The simulations incorporate the experimentally determined material parameters and geometry of the SAF nanoconstriction shown in Fig. 1. They reveal the emergence of self-sustained oscillations when the applied DC current exceeds a critical threshold. To char-

acterize the antiferromagnetic (AF) dynamics, we analyze the time evolution of the net magnetization ($\vec{M} = \vec{M}_1 + \vec{M}_2$), which becomes non-zero only when the magnetizations of the two layers are dynamically canted. Such a canting arises during antiferromagnetic excitations and during the propagation of antiferromagnetic magnons.

Fig. 2 presents representative simulation results illustrating the behavior of the SAF oscillator in different driving regimes at an applied magnetic field of 45 mT along the bar direction. When a subthreshold DC current corresponding to an average current density of $J_{dc}^{below} = 1.7 \times 10^8\ A/cm^2$ at the nanoconstriction, is applied, the damping-like SOT slightly tilts the layer magnetizations along the out-of-plane direction, resulting in a weak and static net magnetization in the constriction (Fig. 2a(i)). The corresponding power spectral density (PSD), computed from the magnetization dynamics in the central nanoconstriction, exhibits no distinct spectral features (Fig. 2b(i)), indicating the absence of self-oscillations.

In contrast, applying a superthreshold DC current density of $J_{dc}^{above} = 2.2 \times 10^8\ A/cm^2$ induces persistent excitations localized in the nanoconstriction region (Fig. 2a(ii)). The associated PSD (Fig. 2b(ii)) shows a broad frequency distribution with an amplitude enhancement near the optical eigenmode frequency of the SAF. These excitations emit propagating spin waves with short wavelengths ($\leq$ 50 nm) radiating from the constriction into the surrounding SAF region. When an additional radio-frequency current density of $J_{RF}^{peak} = 0.5 \times 10^8\ A/cm^2$ at 8 GHz is applied, a portion of the self-oscillatory motion becomes phase-locked to the additional monochromatic RF excitation, as shown in Fig. 2a(iii). This phenomenon, known as injection-locking, leads to a pronounced modification of the spin-wave pattern: longer-wavelength magnons, consistent with the locking frequency of the RF current, dominate the propagation away from the constriction. The corresponding PSD (Fig. 2b(iii)) reveals a sharp peak at the locking frequency, confirming synchronization between the DC driven self-oscillation and the RF current. In the Supplementary Material, we provide two animations in which the antiferromagnetic dynamics and magnon generation due to self-oscillations can be traced without and with injection locking at 8 GHz locking frequency. Importantly, injection locking provides a mechanism for detecting DC-induced self-oscillations via spin rectification, as the synchronized precession component contributes a coherent oscillatory resistance at the RF frequency. This homodyne detection mechanism requires that the spectrum of the SOT-induced excitation contains the RF frequency f_1 and

that the precession remains phase-locked to the RF current [35].

3. Threshold current and emergence of chiral self-oscillations

We now provide experimental evidence for the emergence of self-oscillations near the spin-flop transition, i.e., at low applied magnetic fields ($|\mu_0 H| < 50$ mT), where no resonant eigenmodes are observed in the absence of a DC current [Supplementary Material section 2]. Fig. 3a shows the spin rectification voltage V_{SRE} measured as a function of the applied in-plane magnetic field ($\Phi = 0^o$) for three cases: zero DC current ($I_{dc} = 0$ mA) and finite DC currents of $I_{dc} = \pm 0.45$ mA. The corresponding current density within the nanoconstriction reaches 2.9×10^7 A/cm^2. At zero DC current, no features are observed in the SRE signal at the RF probing frequency of 8 GHz, consistent with the absence of resonant excitation. In contrast, for both positive and negative DC currents, sharp SRE peaks appear at distinct magnetic field values, indicating the onset of resonant excitations. Notably, the sign of these SRE peaks depends solely on the polarity of the applied DC current and reverses when the current direction is inverted.

We attribute these features to self-sustained oscillations driven by the DC current-induced damping-like SOT, which become injection-locked to the fixed RF frequency. The observed current-polarity-dependent SRE signal confirms the chiral nature of these self-oscillations. Since both AMR and GMR are even under simultaneous reversal of $\vec{M}_1$ and $\vec{M}_2$, the sign of the SRE signal does not depend on the polarity of the applied magnetic field but rather on the direction of the driving current. This is consistent with the expected reversal of the spin accumulation at the Pt and Ta interfaces when the DC current is inverted.

Our observations align with the theoretical predictions for in-plane antiferromagnetic spin Hall nano-oscillators, in which the chirality of the self-oscillations is determined by the direction of the applied current [24]. Similar behavior has been reported in compensated ferrimagnetic insulators, where damping-like torque drives and probes the chirality of antiferromagnetic eigenmodes, with the sign of the rectified voltage reflecting the magnon mode chirality [48, 49]. Using Fourier analysis of the time-dependent AMR and GMR responses in our micromagnetic simulations, we numerically confirm that the polarity of the SRE voltage arising from injection-locked self-oscillations is solely determined by the direction of the DC

current and independent of the applied magnetic field (Supplementary Material section 5).

We thus conclude that, in the low-field regime near the spin-flop transition, the chirality of the self-oscillations is uniquely controlled by the DC current polarity, an important distinction from ferromagnetic STT and SOT oscillators, where the chirality is always righthanded with respect to the applied magnetic field [24].

The threshold behavior of the self-oscillations is illustrated in Fig. 3b. Focusing on a representative SRE peak within the narrow field range between –55 mT and –35 mT, we vary the DC current amplitude corresponding to current densities from 0 to $2.9 \times 10^7\ A/cm^2$. The selected SRE peak appears only above a critical current density of $1.3 \times 10^7\ A/cm^2$, and subsequently shifts to lower field values as the current increases further. Notably, the critical current density obtained from micromagnetic simulations is approximately one order of magnitude higher than that observed experimentally. We attribute this discrepancy to the absence of thermal fluctuations in the simulations, which were performed at zero temperature, in contrast to the room-temperature experimental conditions.

4. Current-driven dynamics close to the spin-flop transition with possible signatures of chaotic behavior

To investigate the complex dynamics predicted for spin-orbit torque (SOT)-driven antiferromagnetic oscillators near the spin-flop transition, we performed spin rectification measurements across a range of RF frequencies (5–8 GHz) and compared the acoustic eigenmode of Section 1 with the DC-driven self-excitations described in Section 3. In the absence of a DC current, only the acoustic eigenmode is observed, with a resonance field that shifts monotonically to higher values as the RF frequency increases (Fig. 4a), in agreement with the analytical model discussed in Section 1.

When a DC current with a density exceeding the critical threshold ($J_{\mathrm{dc}}^{\mathrm{above}} = 2.5 \times 10^7\ \mathrm{A/cm^2}$) is applied, a series of additional sharp rectification peaks emerges near zero applied magnetic field, i.e., close to the spin-flop transition (Fig. 4d). These peaks, which are absent under zero DC bias (Fig. 4c), correspond to the injection-locked self-oscillations introduced in Section 3. In contrast to the acoustic eigenmode (Fig. 4b), the field positions of these low-field resonances remain essentially unchanged as the RF frequency is

varied, indicating a fundamentally different form of magnetization dynamics. We attribute this frequency-independent behavior of these injection-locked peaks to a broadband power spectral density (PSD) of the underlying current-driven self-oscillations, consistent with micromagnetic simulation results of Section 2 (c.f., Fig. 2b (ii), (iii)).

To further examine the nature of these excitations, we carried out macrospin simulations using experimentally determined parameters for the RKKY exchange coupling and magnetic anisotropy. While micromagnetic simulations resolve spatial features of the spin dynamics, macrospin simulations enable longer integration times and provide access to the global dynamical behavior over extended timescales and parameter space. The macrospin simulations confirm the emergence of complex and highly nonlinear magnetization dynamics near the spin-flop transition. In particular, Lyapunov exponent analysis and bifurcation diagrams (Supplementary Section 6) reveal both stable and chaotic oscillatory regimes, depending on the applied DC current and magnetic field. These findings are in line with theoretical predictions [26] and suggest that the sudden appearance of multiple resonances above a threshold current, combined with their insensitivity to RF frequency, may indeed be indicative of chaotic self-oscillatory behavior in the SAF system.

Finally, we observe a subtle but systematic dependence of the resonance field of the 8 GHz injection-locked mode on the magnitude of the DC current. As detailed in Supplementary Section 7, increasing the current results in a slight shift ($\approx 1\,\mathrm{mT}$) of the resonance field, further highlighting the current-controlled nature of these excitations.

5. Conclusion

We have demonstrated a spin-orbit torque-driven antiferromagnetic oscillator based on a synthetic antiferromagnet (SAF) nanoconstriction, combining electrical detection with micromagnetic and macrospin simulations. Spin rectification spectroscopy revealed magnetic-field-dependent excitations of linearly polarized acoustic and optical eigenmodes, and, importantly, the emergence of additional resonances that appear only when the applied DC current exceeds a critical threshold.

These additional resonances arise from self-sustained excitations of the antiferromagnetic order, which are absent without the driving DC current. When a radio-frequency (RF) probe

current is superimposed on the DC current, the self-oscillations become injection-locked to the RF frequency and manifest as sharp, field-resonant spin rectification peaks. The sign of the rectified voltage depends solely on the polarity of the DC current, confirming that the oscillation chirality is uniquely determined by the DC current direction, a hallmark feature that distinguishes these antiferromagnetic self-oscillations from their ferromagnetic counterparts.

Micromagnetic simulations, incorporating experimentally determined material parameters and the device geometry, reproduce the emergence of these chiral self-oscillations and their injection locking to the RF probing current. Complementary macrospin simulations, combined with Lyapunov exponent and bifurcation analyses, reveal that oscillators based on the SAF multilayer exhibit both stable and chaotic dynamical regimes near the spin-flop transition. These numerical results support the interpretation that the frequency-insensitive, multi-peak spin rectification response observed above the threshold current may indicate chaotic behavior - a theoretically predicted but previously unobserved characteristic of antiferromagnetic spintronic oscillators.

Together, these results establish synthetic antiferromagnets as a powerful and experimentally accessible platform for exploring ultrafast, chiral, and potentially chaotic spin dynamics. This work also opens new avenues for spintronic oscillator technologies, with the combination of tunable dynamics, broadband operation, and inherent stochasticity offering opportunities for neuromorphic computing, signal processing, and information encoding.

Methods

Sample fabrication

For these studies, we prepared synthetic antiferromagnets (SAFs) consisting of two Py ($Ni_{81}Fe_{19}$) ferromagnetic layers exhibiting easy-plane anisotropy. The antiferromagnetic coupling between these layers was achieved via the Ruderman-Kittel-Kasuya-Yoshida (RKKY) interaction, through a 0.34 nm Ir spacer layer. A 5-nm Ta seedlayer was included underneath the stack to improve adhesion. The whole Ta(5 nm)/Py(2 nm)/Ir(0.34 nm)/Py(2 nm)/Pt(5 nm) multilayer was deposited at room temperature by d.c. magnetron sputtering in an ultrahigh-vacuum BESTEC system. Argon was supplied at a flow of 20 standard cubic centimeters per minute (sccm), resulting in an Ar atmosphere at 0.4 Pa (3 mTorr). The substrates were Si wafers with a 100-nm thermally oxidized SiO_2 layer. During

deposition, the substrate was rotated at ≈60 rpm. The d.c. sputter power was set to 50 W for Py, Pt, and Ta, and 40 W for Ir corresponding to the growth rates of 0.255 nm/s for Py, 0.1 nm/s for Pt, 0.068 nm/s for Ta, and 0.056 nm/s for Ir. Layer thicknesses were controlled via deposition time, and sputter rates were calibrated in advance by X-ray reflectivity.

The constrictions of the devices were defined by electron-beam lithography (EBL) using a positive e-beam resist (AR-P 6200). The exposed regions were etched by argon ion milling in a reactive-ion etching–inductively coupled plasma (RIE–ICP) system. Electrical contacts were fabricated using a standard lift-off process following thermal evaporation of a Cr/Au bilayer (5 nm/80 nm).

Spin rectification effect (SRE) measurements

All electrical SRE measurements were carried out at room temperature. For the SRE measurements, the chip containing the SAF nano-constriction device is mounted on a custom made RF-PCB with coplanar waveguide (CPW) for high frequency access. The SAF nano-constriction device was then bonded to the CPW. A radio frequency (RF) current (I_{RF}) and direct current (I_{DC}) were applied to the device via the high-frequency and low-frequency ports of a bias tee, respectively. For applying the RF current, we used a signal generator, and for the direct current, a precision source measure unit was used. The device, mounted on an RF PCB, was placed inside a room-temperature electromagnet, and the magnetic field was monitored with a Hall sensor and gaussmeter. For the spin rectification effect (SRE) measurements, we employed a field-sweep method, in which the magnetic field was swept at a fixed RF frequency to identify resonances. The RF current driven through the SAF nanoconstriction generates spin–orbit torque and Oersted-field torque, which can both in principle lead to excitation of the Néel order oscillating at the frequency of the RF current. However, in our system, current-induced Oersted-field torque contributions can be neglected due to their magnitude and symmetry. The oscillating Néel order, in turn, produces a time-dependent change in the magnetoresistance (GMR and AMR) of the SAF, which mixes with the RF current to yield a rectified dc voltage V_{SRE}. Because V_{SRE} is very small, we used amplitude modulation of the RF current at 333 Hz and lock-in detection. The device with the RF PCB assembly was mounted on a non-magnetic piezo rotation stage to enable measurements at different in-plane angles.

Micromagnetic simulations

Micromagnetic simulations were performed with MuMax3 [44] on reduced device dimensions of 1 μm $\times$ 0.5 μm with a 70 nm constriction width, scaled from the experimental 15 μm $\times$ 5 μm geometry, preserving the aspect ratios and therefore the asymmetric constriction with 90^o opening angle. Only the magnetization distribution of the two Py layers of the SAF were modeled using MuMax3. Current and Oersted-field distributions were obtained from COMSOL simulations of the same device geometry and used as input for the MuMax3 simulation (Supplementary Note 8). The SAF stack was discretized on a 512 $\times$ 256 $\times$ 3 mesh, corresponding to a cell size of about 2 $\times$ 2 $\times$ 1 nm^3. To suppress artefacts from magnons reflected at the wide leads far from the constriction, Gilbert damping was gradually increased at the outer device regions along with the periodic boundary conditions to mimic the impact of the larger dimensions of the real device. Material parameters were: saturation magnetization $M_s = 7.9 \times 10^5$ A/m, intra-layer exchange stiffness $A = 1.1 \times 10^{-11}$ J/m and a Gilbert damping $\alpha = 0.01$. The interlayer AF coupling was tuned to reproduce experimental spin-flip fields in both in-plane and out-of-plane geometries, giving 0.25 T for the critical field. A spin Hall angle of 0.15 was used to model the SOT. The system was first relaxed to the ground state, then evolved under current and/or field excitation until the steady-state regime was reached.

Data availability

The data of this work are included in the article and it's Supplementary Information. Additional raw data are available from the corresponding authors upon request.

Code availability

The micromagnetic and macrospin simulation codes are available from the corresponding authors upon reasonable request.

Acknowledgements

This work was supported in part by the Deutsche Forschungsgemeinschaft (DFG, German Research Foundation) within Project-ID 314695032 – SFB 1277 "Emergente relativistische Effekte in der Kondensierten Materie", Project-ID 452301518 "Investigation of quench switching of antiferromagnets with high spatial and temporal resolution", and by the European Union's Horizon 2020 research and innovation program under the Marie Skłodowska-Curie Grant Agreement No. 861300 "Cold Opto-Magnetism for Random Access Devices".

The work had also the support from the Czech Science Foundation within the Project GACR 21-28876J. This work was also supported by DFG through Project No. 514946929. DL acknowledges partial financial support from FONDECYT 1240985 and FONDECYT 1231020 as well as from Centers of Excellence with BASAL/ANID financing, CIA250002, CEDENNA.

Author contributions

P.K.R. and J.W. conceived the project. P.K.R., J.G., and J.W. designed the AF-oscillator devices. R.S. and O.H. grew and characterized the SAF multilayers. Z.S. fabricated the nanoconstriction devices. P.K.R., J.G., F.V., C.H.B., and J.W. designed and performed the SRE experiments. P.K.R., F.V., and C.H.B. designed and performed the TR-MOKE experiments. P.K.R. and J.G. carried out the micromagnetic simulations. J.A.V., D.L., and R.M.O. carried out the macrospin simulations. P.K.R., J.G., R.S., R.M.O., and O.G. discussed the relationship between the simulation and experimental results. P.K.R., J.G., and J.W. wrote the manuscript with input from all authors.

---

[1] Torrejon, J. *et al.* Neuromorphic computing with nanoscale spintronic oscillators. *Nature* **547**, 428–431 (2017). URL `http://dx.doi.org/10.1038/nature23011`.

[2] Grollier, J. *et al.* Neuromorphic spintronics. *Nature Electronics* **3**, 360–370 (2020). URL `http://dx.doi.org/10.1038/s41928-019-0360-9`.

[3] Locatelli, N., Cros, V. & Grollier, J. Spin-torque building blocks. *Nature Materials* **13**, 11–20 (2013). URL `http://dx.doi.org/10.1038/nmat3823`.

[4] Romera, M. *et al.* Vowel recognition with four coupled spin-torque nano-oscillators. *Nature* **563**, 230–234 (2018). URL `http://dx.doi.org/10.1038/s41586-018-0632-y`.

[5] Zahedinejad, M. *et al.* Two-dimensional mutually synchronized spin hall nano-oscillator arrays for neuromorphic computing. *Nature Nanotechnology* **15**, 47–52 (2019). URL `http://dx.doi.org/10.1038/s41565-019-0593-9`.

[6] Chen, T. *et al.* Spin-torque and spin-hall nano-oscillators. *Proceedings of the IEEE* **104**, 1919–1945 (2016).

[7] Villard, P. *et al.* A ghz spintronic-based rf oscillator. *IEEE Journal of Solid-State Circuits* **45**, 214–223 (2010).

[8] Chen, T. *et al.* Integration of gmr-based spin torque oscillators and cmos circuitry. *Solid-State Electronics* **111**, 91–99 (2015). URL https://www.sciencedirect.com/science/article/pii/S0038110115001690.

[9] Slonczewski, J. Current-driven excitation of magnetic multilayers. *Journal of Magnetism and Magnetic Materials* **159**, L1–L7 (1996). URL https://www.sciencedirect.com/science/article/pii/0304885396000625.

[10] Berger, L. Emission of spin waves by a magnetic multilayer traversed by a current. *Phys. Rev. B* **54**, 9353–9358 (1996). URL https://link.aps.org/doi/10.1103/PhysRevB.54.9353.

[11] Tsoi, M. *et al.* Excitation of a magnetic multilayer by an electric current. *Phys. Rev. Lett.* **80**, 4281–4284 (1998). URL https://link.aps.org/doi/10.1103/PhysRevLett.80.4281.

[12] Kiselev, S. I. *et al.* Microwave oscillations of a nanomagnet driven by a spin-polarized current. *Nature* **425**, 380–383 (2003). URL http://dx.doi.org/10.1038/nature01967.

[13] Demidov, V. E., Demokritov, S. O., Reiss, G. & Rott, K. Effect of spin-polarized electric current on spin-wave radiation by spin-valve nanocontacts. *Applied Physics Letters* **90**, 172508 (2007). URL https://doi.org/10.1063/1.2732816. https://pubs.aip.org/aip/apl/article-pdf/doi/10.1063/1.2732816/14373921/172508_1_online.pdf.

[14] Deac, A. M. *et al.* Bias-driven high-power microwave emission from mgo-based tunnel magnetoresistance devices. *Nature Physics* **4**, 803–809 (2008). URL http://dx.doi.org/10.1038/nphys1036.

[15] Slavin, A. & Tiberkevich, V. Nonlinear auto-oscillator theory of microwave generation by spin-polarized current. *IEEE Transactions on Magnetics* **45**, 1875–1918 (2009).

[16] Demidov, V. E. *et al.* Magnetic nano-oscillator driven by pure spin current. *Nature Materials* **11**, 1028–1031 (2012). URL http://dx.doi.org/10.1038/nmat3459.

[17] Liu, L., Pai, C.-F., Ralph, D. C. & Buhrman, R. A. Magnetic oscillations driven by the spin hall effect in 3-terminal magnetic tunnel junction devices. *Phys. Rev. Lett.* **109**, 186602 (2012). URL https://link.aps.org/doi/10.1103/PhysRevLett.109.186602.

[18] Liu, R. H., Lim, W. L. & Urazhdin, S. Spectral characteristics of the microwave emission by the spin hall nano-oscillator. *Phys. Rev. Lett.* **110**, 147601 (2013). URL https://link.aps.org/doi/10.1103/PhysRevLett.110.147601.

[19] Demidov, V. E., Urazhdin, S., Zholud, A., Sadovnikov, A. V. & Demokritov, S. O. Nanoconstriction-based spin-Hall nano-oscillator. *Applied Physics Letters* **105**, 172410

(2014). URL https://doi.org/10.1063/1.4901027. https://pubs.aip.org/aip/apl/article-pdf/doi/10.1063/1.4901027/14306507/172410_1_online.pdf.

[20] Duan, Z. *et al.* Nanowire spin torque oscillator driven by spin orbit torques. *Nature Communications* **5** (2014). URL http://dx.doi.org/10.1038/ncomms6616.

[21] Haidar, M. *et al.* A single layer spin-orbit torque nano-oscillator. *Nature Communications* **10** (2019). URL http://dx.doi.org/10.1038/s41467-019-10120-4.

[22] Fulara, H. *et al.* Giant voltage-controlled modulation of spin hall nano-oscillator damping. *Nature Communications* **11** (2020). URL http://dx.doi.org/10.1038/s41467-020-17833-x.

[23] Choi, J.-G. *et al.* Voltage-driven gigahertz frequency tuning of spin hall nano-oscillators. *Nature Communications* **13** (2022). URL http://dx.doi.org/10.1038/s41467-022-31493-z.

[24] Cheng, R., Xiao, D. & Brataas, A. Terahertz antiferromagnetic spin hall nano-oscillator. *Phys. Rev. Lett.* **116**, 207603 (2016). URL https://link.aps.org/doi/10.1103/PhysRevLett.116.207603.

[25] Troncoso, R. E., Rode, K., Stamenov, P., Coey, J. M. D. & Brataas, A. Antiferromagnetic single-layer spin-orbit torque oscillators. *Phys. Rev. B* **99**, 054433 (2019). URL https://link.aps.org/doi/10.1103/PhysRevB.99.054433.

[26] Wolba, B., Gomonay, O. & Kravchuk, V. P. Chaotic antiferromagnetic nano-oscillator driven by spin torque. *Phys. Rev. B* **104**, 024407 (2021). URL https://link.aps.org/doi/10.1103/PhysRevB.104.024407.

[27] Parthasarathy, A., Cogulu, E., Kent, A. D. & Rakheja, S. Precessional spin-torque dynamics in biaxial antiferromagnets. *Phys. Rev. B* **103**, 024450 (2021). URL https://link.aps.org/doi/10.1103/PhysRevB.103.024450.

[28] Gomonay, O., Baltz, V., Brataas, A. & Tserkovnyak, Y. Antiferromagnetic spin textures and dynamics. *Nature Physics* **14**, 213–216 (2018). URL http://dx.doi.org/10.1038/s41567-018-0049-4.

[29] Han, J., Cheng, R., Liu, L., Ohno, H. & Fukami, S. Coherent antiferromagnetic spintronics. *Nature Materials* **22**, 684–695 (2023).

[30] Jungwirth, T., Marti, X., Wadley, P. & Wunderlich, J. Antiferromagnetic spintronics. *Nature Nanotechnology* **11**, 231–241 (2016). URL https://doi.org/10.1038/nnano.2016.18.

[31] Williamson, S. J. & Foner, S. Antiferromagnetic resonance in systems with dzyaloshinsky-moriya coupling; orientation dependence in αfe$_2$o$_3$. *Phys. Rev.* **136**, A1102–A1106 (1964).

URL https://link.aps.org/doi/10.1103/PhysRev.136.A1102.

[32] Keffer, F. & Kittel, C. Theory of antiferromagnetic resonance. *Phys. Rev.* **85**, 329–337 (1952). URL https://link.aps.org/doi/10.1103/PhysRev.85.329.

[33] Khymyn, R. *et al.* Ultra-fast artificial neuron: generation of picosecond-duration spikes in a current-driven antiferromagnetic auto-oscillator. *Scientific Reports* **8** (2018). URL http://dx.doi.org/10.1038/s41598-018-33697-0.

[34] Harder, M., Gui, Y. & Hu, C.-M. Electrical detection of magnetization dynamics via spin rectification effects. *Physics Reports* **661**, 1–59 (2016). URL https://www.sciencedirect.com/science/article/pii/S0370157316303167. Electrical detection of magnetization dynamics via spin rectification effects.

[35] Sakamoto, S. *et al.* Antiferromagnetic spin-torque diode effect in a kagome Weyl semimetal. *Nature Nanotechnology* (2024). URL http://dx.doi.org/10.1038/s41565-024-01820-0.

[36] Choi, J. & Kim, P. Critical neuromorphic computing based on explosive synchronization. *Chaos: An Interdisciplinary Journal of Nonlinear Science* **29**, 043110 (2019). URL https://doi.org/10.1063/1.5086902. https://pubs.aip.org/aip/cha/article-pdf/doi/10.1063/1.5086902/14621310/043110_1_online.pdf.

[37] Marković, D. *et al.* Reservoir computing with the frequency, phase, and amplitude of spin-torque nano-oscillators. *Applied Physics Letters* **114**, 012409 (2019). URL https://doi.org/10.1063/1.5079305. https://pubs.aip.org/aip/apl/article-pdf/doi/10.1063/1.5079305/19751429/012409_1_online.pdf.

[38] Duine, R. A., Lee, K.-J., Parkin, S. S. P. & Stiles, M. D. Synthetic antiferromagnetic spintronics. *Nature Physics* **14**, 217–219 (2018). URL https://doi.org/10.1038/s41567-018-0050-y.

[39] Dyakonov, M. & Perel, V. Current-induced spin orientation of electrons in semiconductors. *Physics Letters A* **35**, 459–460 (1971). URL https://www.sciencedirect.com/science/article/pii/0375960171901964.

[40] Hirsch, J. E. Spin Hall Effect. *Phys. Rev. Lett.* **83**, 1834–1837 (1999). URL https://link.aps.org/doi/10.1103/PhysRevLett.83.1834.

[41] Wunderlich, J., Kaestner, B., Sinova, J. & Jungwirth, T. Experimental observation of the spin-hall effect in a two-dimensional spin-orbit coupled semiconductor system. *Phys. Rev. Lett.* **94**, 047204 (2005). URL https://link.aps.org/doi/10.1103/PhysRevLett.94.047204.

[42] Fang, D. *et al.* Spin–orbit-driven ferromagnetic resonance. *Nature Nanotechnology* **6**, 413–417 (2011). URL http://dx.doi.org/10.1038/nnano.2011.68.

[43] Liu, L., Moriyama, T., Ralph, D. C. & Buhrman, R. A. Spin-torque ferromagnetic resonance induced by the spin hall effect. *Phys. Rev. Lett.* **106**, 036601 (2011). URL https://link.aps.org/doi/10.1103/PhysRevLett.106.036601.

[44] Vansteenkiste, A. *et al.* The design and verification of mumax3. *AIP Advances* **4**, 107133 (2014). URL https://doi.org/10.1063/1.4899186. https://pubs.aip.org/aip/adv/article-pdf/doi/10.1063/1.4899186/12878560/107133_1_online.pdf.

[45] Dai, C. & Ma, F. Strong magnon–magnon coupling in synthetic antiferromagnets. *Applied Physics Letters* **118**, 112405 (2021). URL https://doi.org/10.1063/5.0041431.

[46] Wang, Y. *et al.* Ultrastrong to nearly deep-strong magnon-magnon coupling with a high degree of freedom in synthetic antiferromagnets. *Nature Communications* **15** (2024).

[47] Liu, Y. *et al.* Design of controllable magnon frequency comb in synthetic ferrimagnets. *Phys. Rev. B* **109**, 174412 (2024). URL https://link.aps.org/doi/10.1103/PhysRevB.109.174412.

[48] Wang, L. *et al.* Electrical Excitation and Detection of Chiral Magnons in a Compensated Ferrimagnetic Insulator. *Physical Review Letters* **133**, 166705 (2024). URL https://doi.org/10.1103/PhysRevLett.133.166705.

[49] Shiota, Y., Taniguchi, T., Hayashi, D. & Narita, H. Handedness manipulation of propagating antiferromagnetic magnons. *Nature Communications* 1–18 (2024). URL http://dx.doi.org/10.1038/s41467-024-54125-0.

Figure Captions

Fig. 1 Spin-orbit torque-driven excitation of acoustic and optical eigenmodes.

a), Schematic of the SAF multilayer comprising two permalloy (Py : $Ni_{0.81}Fe_{0.19}$) layers antiferromagnetically coupled via a 0.34-nm Ir spacer, sandwiched between Pt and Ta layers. The green arrows indicate the spin polarization directions injected from the heavy-metal interfaces when a charge current flows through the multilayer stack. Red and blue arrows represent the magnetization vectors ($\vec{M}_1$) and ($\vec{M}_2$) of the upper and lower Py layers, respectively. The in-plane magnetic field ($\vec{H}$) and charge current ($\vec{J}$) are applied at an angle Φ. **b)**, Scanning electron micrograph of a fabricated nanoconstriction device with a constriction width (w) of approximately 170 nm. **c)**, Illustration of the magnetization dynamics for the acoustic mode (top, excited at $\Phi = 0^o$) and optical mode (bottom, excited at $\Phi = 90^o$). The acoustic mode corresponds to in-plane precession of the net magnetization ($\vec{M} = \vec{M}_1 + \vec{M}_2$), while the optical mode corresponds to out-of-plane precession. **d)**, Spin rectification voltage V_{SRE} measured as a function of magnetic field for $\Phi = 0^o$, 45^o, and 90^o at 8 GHz and 15 dBm RF power. Depending on Φ, the data show either selective or combined excitation of acoustic and optical modes. **e)**, V_{SRE} versus magnetic field for different RF frequencies from 2 GHz to 12 GHz, showing the frequency dependence of the acoustic mode. **f)**, Extracted resonance frequencies of the acoustic (red symbols) and optical (blue symbols) modes versus magnetic field. Solid and dashed black lines follow the analytical mode frequencies for easy-plane antiferromagnets using the values $\mu_0 H_{ex} = 0.25$ T and $\mu_0 H_{an} = 0.98$ T, determined independently from VSM measurements. The star corresponds to the measurements of (d) for 8 GHz.

Fig. 2 Micromagnetic simulations of SOT driven self-oscillations.

a), Time-snapshots of normalized net-magnetization at **(i)** J_{dc}^{below}, **(ii)** J_{dc}^{above}, and **(iii)** J_{dc}^{above} + J^{RF} . **b)**, Power spectral densities (PSD) at the three different bias conditions. (J_{dc}^{below} = 1.7×10^8 A/cm^2, J_{dc}^{above} = 2.2×10^8 A/cm^2; $J_{RF} = Asin(2\pi ft)$ with f= 8 GHz, A= 0.5×10^8 A/cm^2; $m_z = \hat{z}.(\vec{M}_1 + \vec{M}_2)/(|\vec{M}_1| + |\vec{M}_2|)$. During the simulations, a small magnetic

field of 45 mT is applied along the bar direction.

Fig. 3 SRE detection of dc current induced self-oscillations in SAF.

a), Electrical measurements of the SRE signal for self-oscillations vs. applied magnetic field for three different dc current densities; 0 (black), $-2.9 \times 10^7\ A/cm^2$ (blue) and $+2.9 \times 10^7\ A/cm^2$ (red) with RF current at 8 GHz and 15 dBm. The two chiralities of self-oscillation modes, left-handed mode (LHM) and right handed mode (RHM), are shown as schematic. **b)**, DC current density dependencies of a single self-oscillation mode from 0 A/cm^2 to $2.9 \times 10^7\ A/cm^2$ showing the threshold behavior of self-oscillation. The magnetic field in this case is applied along the bar direction ($\Phi = 0^o$).

Fig. 4 Frequency dependencies of the injection-locked self-oscillations in SAF.

a) and **b)** show the acoustic modes for frequencies between 5 GHz to 8 GHz and with $J_{dc} = 0$ and $J_{dc} = +2.9 \times 10^7\ A/cm^2$ respectively obtained from the SRE measurements. The SRE measurements with the injection-locked self-oscillations for frequencies from 5 GHz to 8 GHz are shown in **c)** and **d)** for $J_{dc} = 0$ and $J_{dc} = +2.9 \times 10^7\ A/cm^2$ respectively. In **c)** and **d)**, the measured SRE voltages are shifted along y-axis for different frequencies for better visualizations of the self-oscillation modes. The magnetic field is applied along the bar direction with a slight misalignment and the RF power for all the frequencies was kept fixed at 15 dBm.

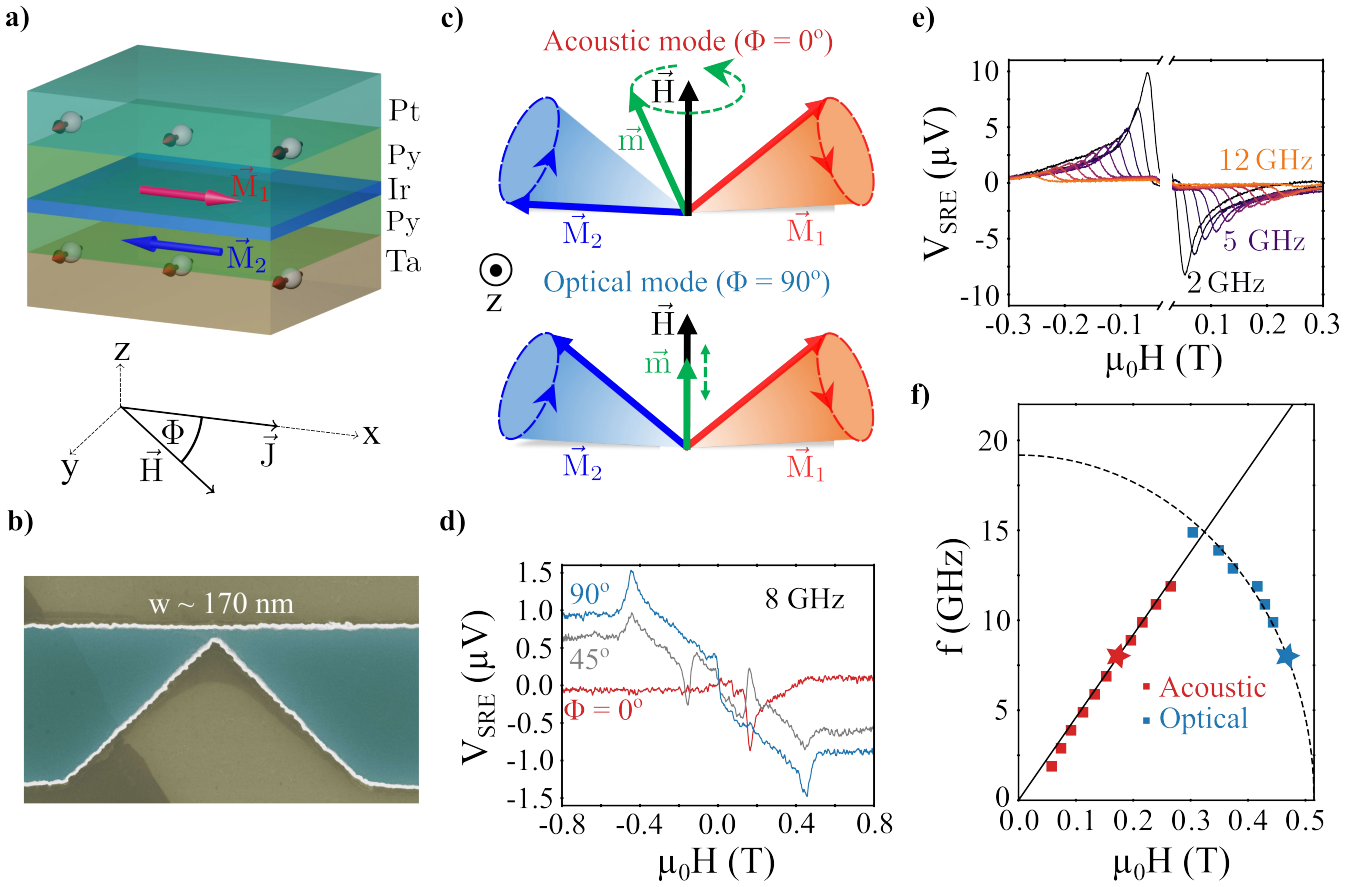

a)
Pt
Py
Ir
Py
Ta
$\vec{M}_1$
$\vec{M}_2$
z
y
x
$\vec{H}$
Φ
$\vec{J}$
b)
w ~ 170 nm
c)
Acoustic mode (Φ = 0°)
$\vec{H}$
$\vec{m}$
$\vec{M}_2$
$\vec{M}_1$
z
Optical mode (Φ = 90°)
d)
90°
8 GHz
45°
Φ = 0°
V_{SRE} (μV)
$\mu_0 H$ (T)
e)
12 GHz
5 GHz
2 GHz
V_{SRE} (μV)
$\mu_0 H$ (T)
f)
f (GHz)
Acoustic
Optical
$\mu_0 H$ (T)

FIG. 1.

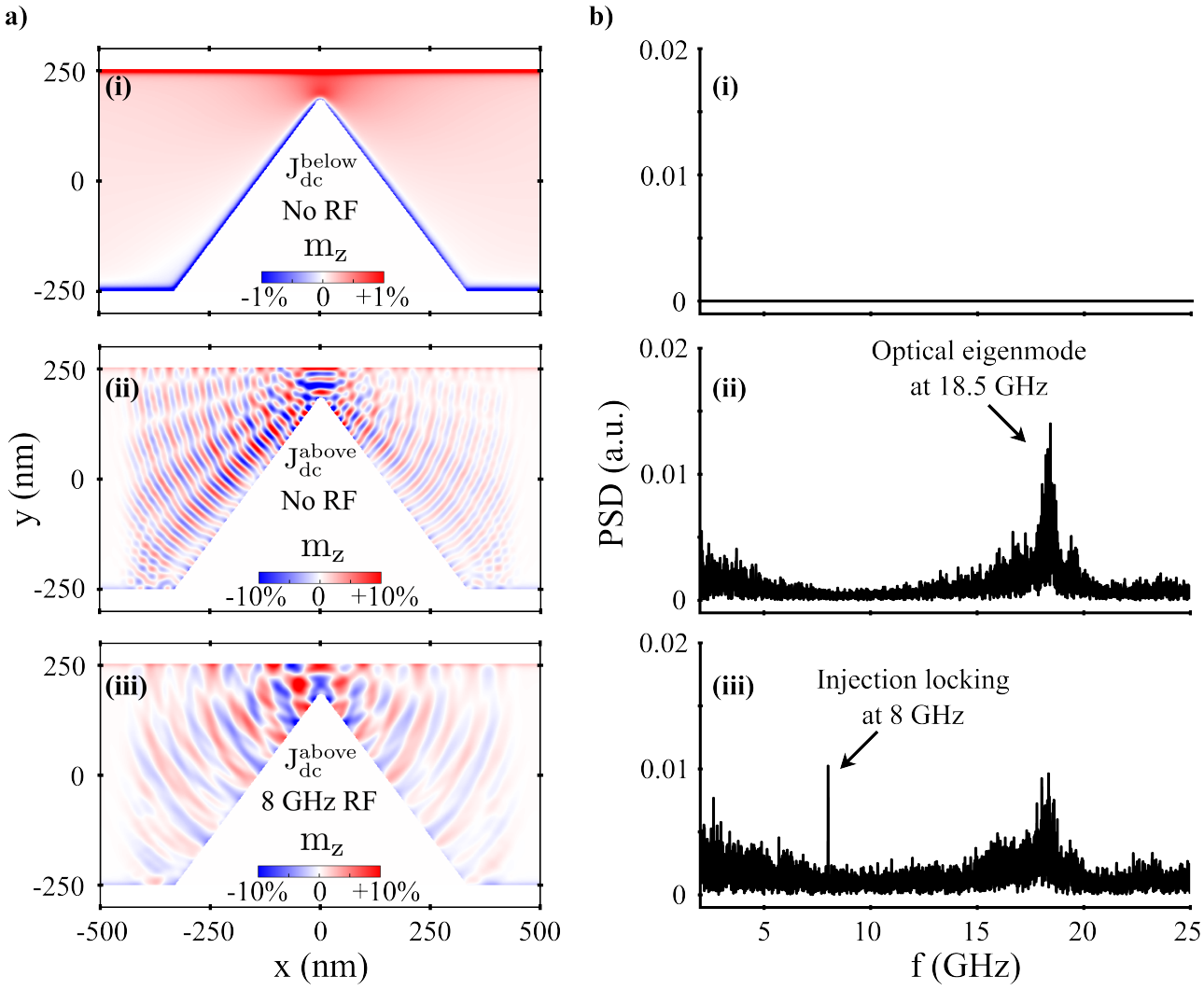

a)
b)
(i)
(ii)
(iii)
J_{dc}^{below}
No RF
m_z
-1% 0 +1%
J_{dc}^{above}
No RF
m_z
-10% 0 +10%
J_{dc}^{above}
8 GHz RF
m_z
-10% 0 +10%
y (nm)
x (nm)
PSD (a.u.)
f (GHz)
Optical eigenmode
at 18.5 GHz
Injection locking
at 8 GHz

FIG. 2.

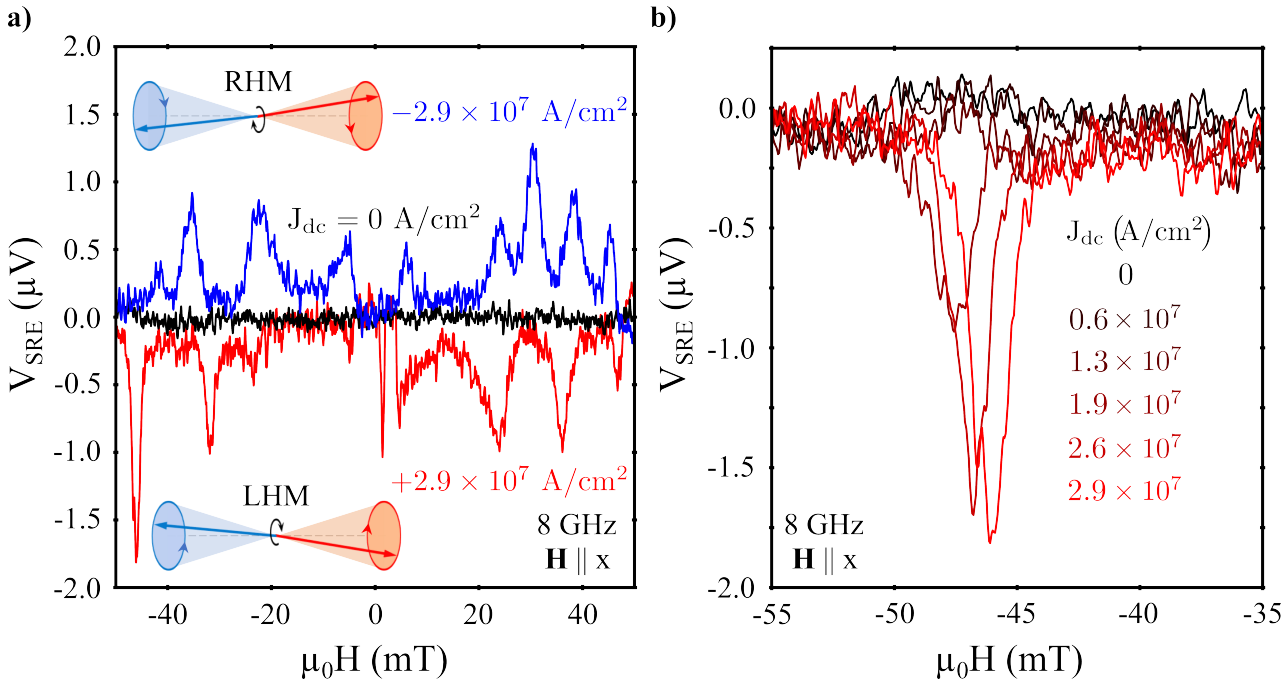

a)
b)
RHM
-2.9×10^7 A/cm^2
$J_{dc} = 0$ A/cm^2
$+2.9 \times 10^7$ A/cm^2
LHM
8 GHz
H || x
V_{SRE} (μV)
μ_0H (mT)
J_{dc} (A/cm^2)
0
0.6×10^7
1.3×10^7
1.9×10^7
2.6×10^7
2.9×10^7
8 GHz
H || x

FIG. 3.

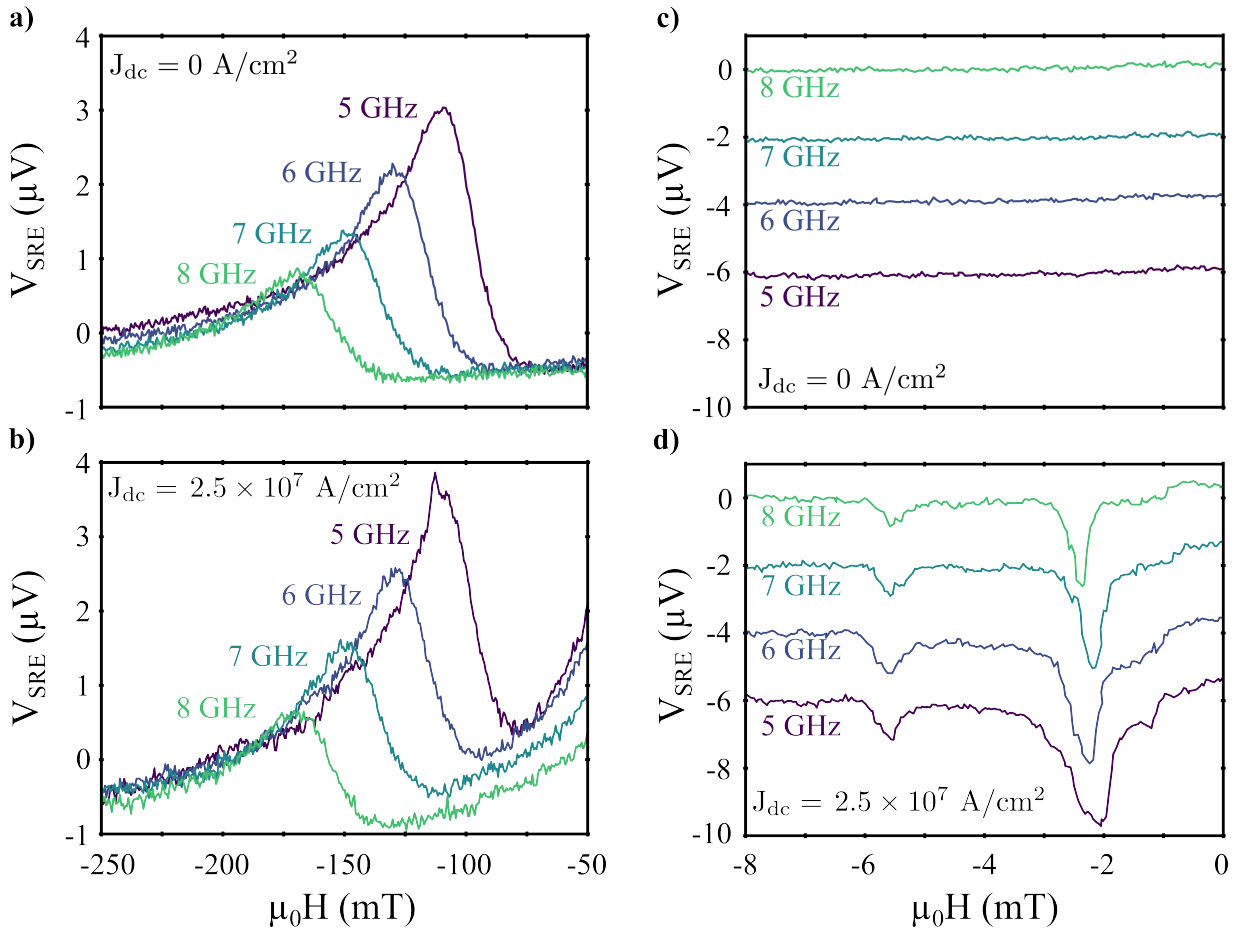

a)
b)
c)
d)
$J_{dc} = 0$ A/cm^2
$J_{dc} = 2.5 \times 10^7$ A/cm^2
5 GHz
6 GHz
7 GHz
8 GHz
V_{SRE} (μV)
μ_0H (mT)

FIG. 4.

Supplementary Files

This is a list of supplementary files associated with this preprint. Click to download.

- SupplementaryMovie1OnlyDCdrivenselfoscillation.mp4
- SupplementaryMovie2DCdrivenselfoscillationwith8GHzRFlocking.mp4
- suppldraft.pdf